

pubs.acs.org/cm Article

Prediction and Kinetic Stabilization of Sn(II)-Perovskite Oxide Nanoshells

Shaun O'Donnell, D. J. Osborn, Gowri Krishnan, Theresa Block, Aylin Koldemir, Thomas D. Small, Rachel Broughton, Jacob L. Jones, Rainer Pöttgen, Gunther G. Andersson, Gregory F. Metha, and Paul A. Maggard*



Cite This: Chem. Mater. 2022, 34, 8054-8064



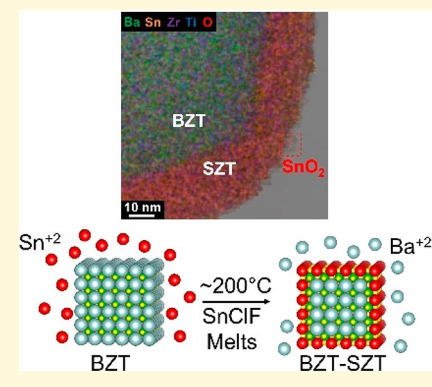
ACCESS

III Metrics & More

Article Recommendations

Supporting Information

ABSTRACT: The synthesis of kinetically stabilized, i.e., metastable, dielectric semiconductors, represents a major frontier within technologically important fields as compared to thermodynamically stable solids that have received considerably more attention. Of long-standing theoretical interest are Sn(II) perovskites [e.g., $Sn(Zr_{1/2}Ti_{1/2})O_3$ (SZT)], which are isoelectronic Pb-free analogues of $Pb(Zr_{1/2}Ti_{1/2})O_3$ (PZT), a commercial piezoelectric composition that is dominant in the electronics industry. Herein, we describe the synthesis of this metastable SZT dielectric through a low-temperature flux reaction technique. The SZT has been found, for the first time, to grow and to be stabilized as a nanoshell at the surfaces of $Ba(Zr_{1/2}Ti_{1/2})O_3$ (BZT) particles, i.e., forming as BZT–SZT core–shell particles, as a result of Sn(II) cation exchange. In situ powder X-ray diffraction (XRD) and transmission electron microscopy data show that the SZT nanoshells result from the controlled cation diffusion of Sn(II) cations into the BZT particles, with tunable thicknesses of $\sim\!25\!-100$ nm. The SZT nanoshell is calculated to possess a metastability of approximately -0.5 eV atom $^{-1}$ with



respect to decomposition to SnO, ZrO_2 , and TiO_2 and cannot currently be prepared as stand-alone particles. Rietveld refinements of the XRD data are consistent with a two-phase BZT–SZT model, with each phase possessing a generally cubic perovskite-type structure and nearly identical lattice parameters. Mössbauer spectroscopic data (^{119}Sn) are consistent with Sn(II) cations within the SZT nanoshells and an outer $\sim 5-10$ nm surface region comprised of oxidized Sn(IV) cations from exposure to air and water. The optical band gap of the SZT shell was found to be ~ 2.2 eV, which is red-shifted by ~ 1.2 eV compared to that of BZT. This closing of the band gap was probed by X-ray photoelectron spectroscopy and found to stem from a shift of the valence band edge to higher energies (~ 1.07 eV) as a result of the addition of the Sn $5s^2$ orbitals forming a new higher-energy valence band. In summary, a novel synthetic tactic is demonstrated to be effective in preparing metastable SZT and representing a generally useful strategy for the kinetic stabilization of other predicted, metastable dielectrics.

I. INTRODUCTION

Synthetic advances in the preparation of metal oxides have led to the discovery of thousands of new compounds that have made a tremendous impact in a wide range of fields, including dielectrics, ferroelectrics, magnetic materials, and photocatalysts. A predominant majority of known metal oxides have been synthesized using traditional high-temperature ceramic methods, thereby favoring the formation of thermodynamically stable compounds. In more recent years, the prediction of thermodynamically unstable oxides has received more attention for their potential to show new and/ or enhanced physical and chemical properties. 1-3 While the possible advantages of metastable oxides have long been theorized, in practice, their syntheses have proven to be challenging. Frequently, the synthesis of metastable oxides has relied upon serendipity or simple trial-and-error approaches. Considering this high degree of difficulty, metastable oxides have therefore remained significantly underexplored. However,

the number of metastable metal oxides that can potentially be kinetically stabilized has been predicted to far exceed those that are thermodynamically stable and currently known.^{4,5}

Some metal oxide systems are well-known to exhibit very few or no thermodynamically stable phases, such as those systems containing In(I), Cu(I), and Sn(II) cations. This is the result of their preference for coordination environments (e.g., linear or asymmetric as a result of a stereoactive lone pair) that act to destabilize most of the common structure types of metal oxides, thus leading to their decomposition to simpler oxides. However, recent large-scale computational studies have

Received: July 20, 2022 Revised: August 22, 2022 Accepted: August 23, 2022

Published: August 30, 2022





demonstrated that semiconductors in these systems have the potential to possess desirable properties such as high charge carrier mobility, defect tolerance, and small band gaps. Research in the Maggard and Jones groups has led to the discovery of promising new routes to the synthesis of metastable perovskites by the flux-based topotactic transformation of structural precursors with high cohesive energies that aid in their kinetic stabilization. 8,9 For example, a highly facile exchange of Sn(II) on the A site of the perovskite structure was found using a low-melting SnClF peritectic flux, such as in the synthesis of $Ba_{1-x}Sn_xZrO_3$ (x = 0 to ~0.6). These new Sn(II)-containing oxide semiconductors show a high metastability, with a calculated $\Delta E_{\rm decomp}$ of up to $-0.3~{\rm eV}$ atom⁻¹. Their kinetic stabilization is achieved by inhibition of phase segregation and the relatively low reaction temperatures. In these cases, significantly red-shifted band gaps down to \sim 2.0 eV are found with increasing metastability, as well as increased rates of photocatalytic oxidation of water to molecular oxygen.8 However, a pure Sn(II) perovskite oxide has yet to be reported as a result of their metastability.

Perovskite oxides with compositions close to Sn(Zr_{0.5}Ti_{0.5})-O₃ have long been recognized as a technologically important dielectrics, as they represent Pb-free analogues of the commercial $Pb(Zr_{1-y}Ti_y)O_3$ piezoelectric. Despite this recognition, the synthesis of Sn(Zr_{0.5}Ti_{0.5})O₃ had not yet been achieved owing to the associated challenges of SnO as a reactant, the ease of oxidation of Sn(II) to Sn(IV) in air, and its rapid disproportionation to SnO₂ and Sn at temperatures as low as ~300 °C. 13,14 The difficulty in preparing this Sn(II) perovskite oxide also stems from its high degree of metastability toward decomposition to the binary oxides, e.g., $2Sn(Zr_{0.5}Ti_{0.5})O_3 \rightarrow 2SnO + ZrO_2 + TiO_2$. Additionally, in the case of SnTiO₃, there is a more stable polymorph with an ilmenite-type structure that has been experimentally prepared and is borderline thermodynamically stable. 15 Given these synthetic barriers, described herein is the remarkable synthesis and investigation of the Sn(II)-containing perovskite oxide Sn(Zr_{0.5}Ti_{0.5})O₃ obtained from a low-temperature cationexchange reaction as a nanoshell covering Ba(Zr_{0.5}Ti_{0.5})O₃ particles.

II. EXPERIMENTAL SECTION

lla. Synthetic Procedure. The BZT particles were prepared via grinding stoichiometric amounts of $BaCO_3$ (Alfa Aesar, 99.8%), TiO_2 (J. T. Baker, >99%), and ZrO_2 (Beantown Chemical, 99.5%) with a 10% molar excess of $BaCO_3$. Next, an equimolar mixture of NaCl and KCl was added to serve as an eutectic flux with a salt:product ratio of 20:1, and thereby lower the reaction temperature. This mixture was subsequently ground for 20 min. The reactants were heated to 1100 °C and held for 24 h before radiative cooling to room temperature. The BZT product was repeatedly washed with deionized water to remove the remaining flux.

A 40% Sn-containing composition, i.e., 0.6 BZT-0.4 SZT, was prepared by grinding BZT with stoichiometric amounts of SnCl₂ (Alfa Aesar, 99% minimum) and SnF₂ (Alfa Aesar, 97.5%) in a glovebox under an Ar atmosphere. The resulting powder was loaded into a fused silica tube and sealed under dynamic vacuum. The mixture was heated to 350 °C at a rate of 12 °C min $^{-1}$, held for 12 h, and then allowed to radiatively cool to room temperature inside the furnace. The final products were washed multiple times with deionized water to remove BaClF and any unreacted SnClF and then allowed to dry at 80 °C overnight. A 20% Sn-containing composition was similarly prepared.

IIb. Characterization. Powder X-ray diffraction (XRD) patterns were measured on a PANalytical Empyrean X-ray diffractometer

operating with Cu K\$\alpha\$ radiation (45 kV, 40 mA) with a step size of 0.0131° in 2\$\theta\$. The data were refined via the Rietveld method using the GSAS-II software package, as a check of both the overall structure type, lattice parameters, and site occupancies. \$^{16}\$ Temperature-dependent XRD data were also measured in situ under the same conditions of a typical reaction, i.e., as the BZT and SnCl2/SnF2 reactants were heated from 25 to 375 °C within a sealed capillary under an Ar atmosphere. An initial room-temperature data set was taken, which was followed by a second data set taken at 250 °C. Subsequent data sets were taken in 10 °C intervals up to 380 °C. The dwell time for each step was 50 min.

The high-angle annular dark-field scanning TEM (HAADF-STEM) and energy-dispersive X-ray spectroscopy (STEM-EDS) elemental maps of BZT-SZT core-shell particles were recorded with a FEI Titan Themis STEM instrument operating at 200 keV and equipped with a Super-X EDS detector in conjunction with a low-background sample holder to minimize Cu background peaks and maximize X-ray collection efficiency. EDS data were analyzed using the Velox software from Thermo Fisher Scientific. Samples were prepared by dropping freshly prepared dispersions of as-prepared material in Milli-Q water (sonicated until dispersed) onto a 300 mesh copper grid with a lacey carbon support film. The water was then allowed to evaporate before the sample was placed in the sample holder. Focused ion beam (FIB) slicing to obtain the STEM-EDS cross section of BZT-SZT coreshell particles was obtained by adhering a small sample of powder to a holder using Pt. The sample was milled on two parallel sides using a focused Ga ion beam to form a wafer that was then transferred to a copper TEM grid holder for imaging.

Ultraviolet—visible (UV—vis) diffuse reflectance data were measured on a Shimadzu UV-3600 instrument equipped with an integrating sphere to probe the onset of optical absorption and band gap sizes. The data were transformed using the Kubelka—Munk, F(R), function. The Apressed barium sulfate disc served as the background. A $Ca^{119m}SnO_3$ source was used for Mössbauer spectroscopic experiments on the samples reacted with 40% Sn(II) cations, $(Ba_{0.6}Sn_{0.4})$ - $(Zr_{0.5}Ti_{0.5})O_3$, and 20% Sn(II) cations, $(Ba_{0.8}Sn_{0.2})(Zr_{0.5}Ti_{0.5})O_3$. The measurements were carried out in a standard liquid nitrogen bath cryostat at 78 K. The source was kept at room temperature. The sample was mixed with α -quartz and enclosed in small PMMA containers at an optimized thickness. Fitting of the data was performed by using the WinNormos for Igor6 program package. Samples were further characterized by XPS methods.

The electron spectroscopy instrument is described in detail in refs 20 and 21 and has a base pressure of 10^{-10} mbar. The Mg K line (12 kV, 200 W) of a nonmonochromatic X-ray source was used for XPS. The angle of observation, i.e., the angle between the source and the analyzer, is 54°. Survey scans were recorded at a pass energy of 40 eV and were followed by high-resolution scans at a pass energy of 10 eV for all core electron spectra of all elements constituting the samples and the valence electron spectra. XPS has a probing depth of ~10 nm and allows the identification of the relative concentration and chemical states of an element. The samples were charging during the acquisition of electron spectroscopy data, and an electron-compensation flood gun was used when analyzing the samples to compensate for the charging. The XP spectra were calibrated by setting the Ti⁴⁺ peak to 458.8 eV, which is close to the binding energy found for TiO₂ samples.

Ilc. Electronic Structure and Total Energy Calculations. Density functional theory methods were implemented as employed in the *Vienna Ab Initio Simulation Package* (VASP; version 4.6) to calculate the predicted, geometry-relaxed structure of $Sn(Zr_{0.5}Ti_{0.5})O_3$ (SZT) and its total energy. ^{22,23} To model its chemical composition with disordered Ti/Zr atoms on the B site of the perovskite structure, superstructures were created with dimensions of $4 \times 4 \times 4$ of the original cubic unit cell [space group $Pm\bar{3}m$ (No. 221)]. The superstructure contained a total of 64 Ti/Zr sites, and the B-site atoms randomly placed within it, giving the SZT composition. Perdew—Burke—Ernzerhof functionals were utilized within the generalized gradient approximation and the projector-augmented wave method. The Brillouin zone was automatically sampled using a 2

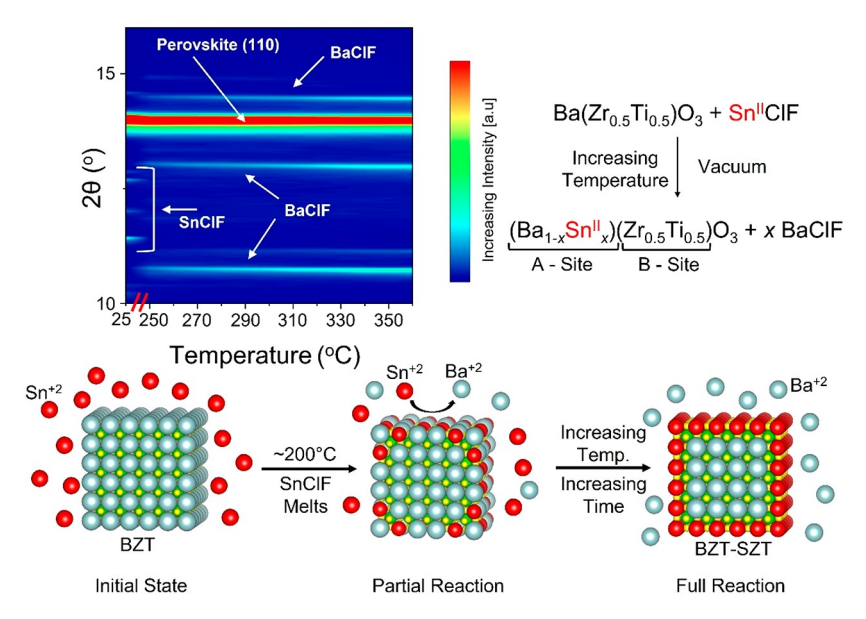


Figure 1. In situ powder XRD of the Sn(II)-exchange reaction (top) upon heating from room temperature to ~375 °C and schematic of the Sn(II) exchange occurring at the BZT particles' surfaces (bottom).

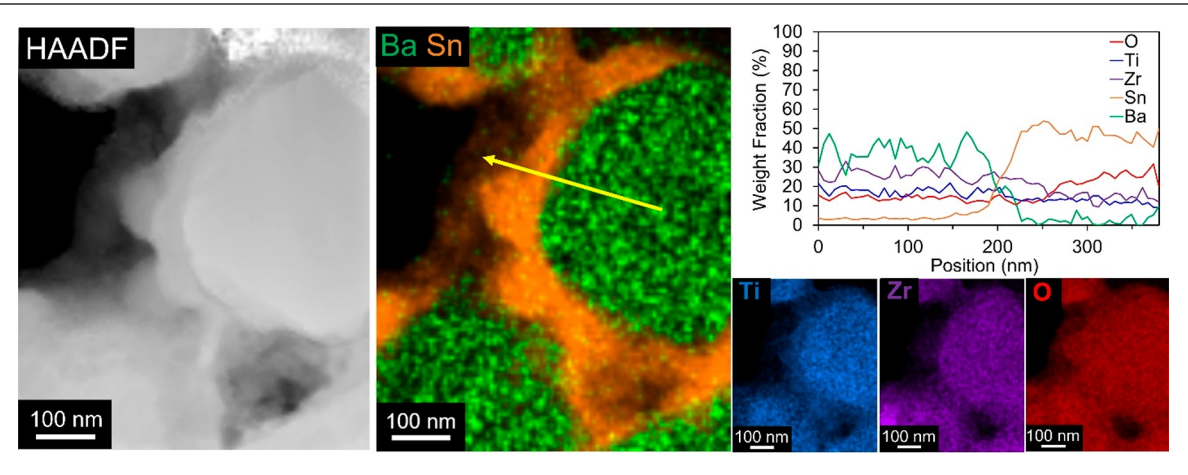


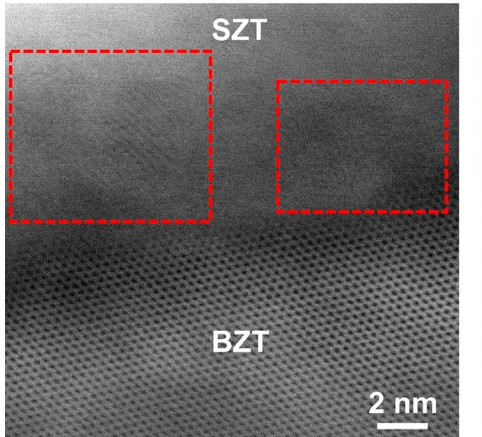
Figure 2. HAADF, EDS maps, and line scan of core—shell BZT—SZT particles, after FIB cutting, revealing particles formed with a Ba-containing core and Sn-containing shell. Color maps show the segregated Ba-core and Sn-shell areas, with elemental contributions of O, Ti, and Zr shown throughout the particles. A line scan (top right) across a single particle shows the segregation of Ba- and Sn-containing regions.

 $\times~2~\times~2$ Monkhorst–Pack grid. The unit cell and the Sn positions were fully geometry relaxed (no symmetry restrictions), with 10^{-6} and 10^{-2} set as the energy and ionic-step convergence criteria, respectively. Total internal energy calculations were utilized to calculate the stability of SZT against decomposition to the simpler oxides, e.g., TiO $_2$, SnO, and ZrO $_2$ using methods as established previously. $^{8,24,2.5}$ The formation energies of the metal oxides were benchmarked for consistency against values found in the Open Quantum Materials Database (OQMD), as determined by total energy calculations within VASP at 0 K. 26

III. RESULTS AND DISCUSSION

Illa. Synthesis and Structural Characterization of BZT-SZT Core-Shell Structure. Upon initial consideration, cation exchange of the A site of a perovskite compound may seem unfeasible because of the relatively densely packed structure. For this reason, layered or porous structures have historically been considered the most suitable for exhibiting facile ion exchange owing to their relatively "open" diffusion pathways. However, there has been a recent renaissance in the use of topotactic ion-exchange reactions in close-packed

structures, which has led to the discovery of a number of new, metastable functional solids.²⁷ The success of these reactions often relies upon the maintenance of the underlying close-packed structure during the exchange process and can be facilitated via the soft, or low-temperature, exchange conditions. Inspired by these prior studies, we investigated the synthesis of core-shell BZT-SZT [Ba(Zr_{0.5}Ti_{0.5})O₃-Sn(Zr_{0.5}Ti_{0.5})O₃] compositions via low-temperature ionexchange reactions, e.g., Ba(Zr_{0.5}Ti_{0.5})O₃ + 0.2SnCl₂ + $0.2SnF_2 \rightarrow 0.6Ba(Zr_{0.5}Ti_{0.5})O_3 - 0.4Sn(Zr_{0.5}Ti_{0.5})O_3 +$ 0.4BaClF. The role of the Sn(II)-based flux, i.e., SnClF, is to facilitate cation mobility at low temperatures without dissolving the underlying perovskite substructure. In situ powder XRD was used to probe the reaction progress, illustrated in Figure 1 (top), and shows the ion-exchange reaction occurs starting at temperatures as low as ~225 °C and continuing up to ~350 °C. Room-temperature powder XRD data show the peaks corresponding to the two reactants, namely, the (110) peak of BZT and SnClF (both labeled in Figure 1). The next data set, taken at 250 °C, shows the



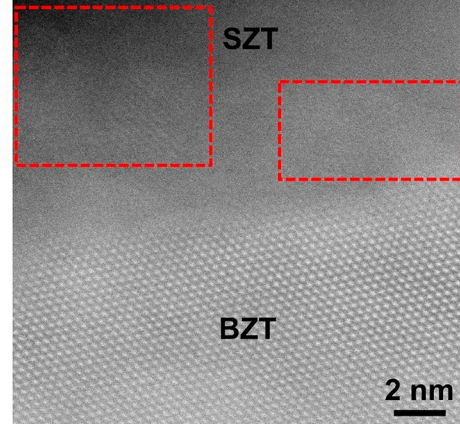


Figure 3. Bright-field and HAADF images of the BZT-SZT core-shell interface showing a single crystalline BZT core and polycrystalline SZT shell. Red boxes indicate observed lattice fringes in the SZT shell.

disappearance of the SnClF peaks (mp ~ 197 °C) and the appearance of three new peaks corresponding to BaClF (mp ~ 1000 °C). This is consistent with the exchange of Sn(II) for Ba(II) beginning at these reaction temperatures. Importantly, the perovskite (110) peak is still present and indicates the maintenance of the underlying B-O substructure of the perovskite during the exchange. As the temperature was increased to 350 °C, there was an increase in the relative intensity of the BaClF peaks, but no new peaks were observed. The mechanism of the exchange of Sn(II) for Ba can be described as shown in Figure 1 (bottom). The first step of the reaction begins at ~200 °C, as SnCl₂/SnF₂ melts and coats the BZT particles. The formation of BaClF from SnClF is exothermic (-1028 kJ mol⁻¹) and serves as the primary thermodynamic driving force for the exchange.²⁸ At higher temperatures, the Sn(II) cations begin to diffuse into the BZT particles and more completely exchange with Ba(II) cations. Attempts to synthesize pure SZT, i.e., 100% Sn, were unsuccessful and resulted in significant decomposition via the formation of SnO and ZrO2. It is also noted that several other reaction temperatures and times were investigated but led to either an incomplete reaction (e.g., temperatures of <350 °C) or decomposition (e.g., temperatures of >350 °C or longer reaction times).

Changes in the chemical composition of the BZT-SZT particles were probed using TEM methods, shown in Figure 2 and Figures S1 and S2. High-resolution images of representative particles reveal the core of the particles to be crystalline and correspond to a Ba-rich region, i.e., Ba(Zr_{0.5}Ti_{0.5})O₃. Also observed was a polycrystalline Sn-containing shell at the surfaces of each particle that is comprised exclusively of Sn, Ti, Zr, and O, having a composition consistent with $Sn(Zr_{0.5}Ti_{0.5})$ -O₃. The polycrystalline nature of the SZT shell can be seen in Figure 3. While the BZT core is single crystalline and aligned with the beam, only certain subregions on the SZT shell are aligned as indicated by the red boxes in Figure 3. To characterize the extent of diffusion of Sn into the particles more fully, representative particles were FIB-cut to characterize their cross sections. Representative images and EDS maps are shown in Figure 2, where there is clear evidence of a Sncontaining shell (orange color) and a Ba-containing core (green color). The line scan clearly illustrates that the weight fraction of Ba sharply decreases starting at ~175 nm from the particle center. Concurrent with the precipitous decrease in Ba

concentration was a parallel increase in the amount of Sn, consistent with the cation substitution of Sn(II) for Ba(II) as found in the powder XRD data. The intraparticle boundary between the Ba core and Sn shell is fairly sharp as there is only an $\sim\!30$ nm region, located $\sim\!190\!-\!220$ nm from the particle center, which contains appreciable amounts of both Ba and Sn. On average, the Sn-containing shell was found to be $\sim\!25\!-\!100$ nm for BZT–SZT core–shell particle sizes ranging from $\sim\!500$ nm to 1 μ m.

The results presented above indicate that, as the SnClF melts and reacts at the particles' surfaces at temperatures as low as 250 °C, the Sn(II) cations exchange with the Ba cations with the exothermic formation of the BaClF salt. However, chemical diffusion is insufficient under these reaction conditions to extend throughout the micrometer-sized particles, thus resulting in a Sn-containing outer shell on all of the BZT particles. Importantly, this suggests that potential routes to the synthesis of pure SZT could be to decrease the primary BZT particle size to better match the Sn diffusion length observed via TEM or, alternatively, to improve the Asite cation diffusion such as through chemical doping. Furthermore, the influence of defects and grain boundaries on the Sn(II) substitution is still being considered and could play an important role in the diffusion of the Sn(II) cation. A small region containing both Ba and Sn indicates that it is possible for both A-site cations to coexist in a disordered, solidsolution-type fashion and that the observation of two distinct regions is simply a consequence of the reaction kinetics. As one can observe in the line scan in Figure 2, the Sn shell also contains both B-site cations, Ti and Zr, as well as O. While the Ti concentration remains relatively constant between the Bacontaining core and Sn-containing shell regions, there is a small observed decrease in Zr concentration and a slight increase in the O concentration when shifting closer to the particles' surfaces. These changes are consistent with a small amount of decomposition and the formation of a small amount of ZrO2 impurity at the surfaces, as observed by powder XRD of samples heated to higher temperatures where the level of decomposition was significantly increased. The increasing O signal intensity at the particle surface could also be the result of small amounts of surface oxidation of Sn(II) to Sn(IV), as is described in more detail below.

To probe the crystalline structures of the $Ba(Zr_{0.5}Ti_{0.5})O_3$ (BZT) core and the $Sn(Zr_{0.5}Ti_{0.5})O_3$ (SZT) shell, powder

XRD data were refined to both a two-phase model (SZT and BZT) and a single-phase model [BSZT; containing mixed Asite cations, i.e., $(Ba_{1-y}Sn_y)Zr_{0.5}Ti_{0.5}O_3$] for comparison. Both phases were modeled as cubic perovskites [space group $Pm\overline{3}m$ (No. 221)]. Final refined parameters are listed in Table 1, and

Table 1. Refinement Results of XRD Data from the One-Phase and Two-Phase Models

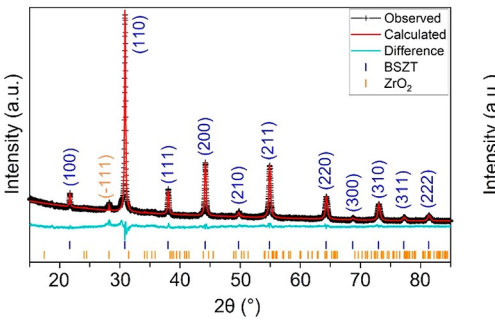
	one phase	two phases	
parameter	BSZT	BZT	SZT
lattice parameter (Å)	4.0927(1)	4.0963(1)	4.088(1)
$R_{\rm w}$ (%)	3.65	3.55	
phase fraction	0.99	0.59	0.40
Ba fraction	0.61(6)	1.00 ^a	0.00^{a}
Sn fraction	0.39(6)	0.00 ^a	1.00 ^a
Zr fraction	0.491(7)	0.55(3)	0.461(1)
Ti fraction	0.509(7)	0.45(3)	0.53(1)
^a Value not refined.			

comparisons of the modeled and measured diffraction data are plotted in Figure 4. Given that both models represent a similar overall A-site ratio of the Ba and Sn atoms, they naturally lead to relatively equally good fits of the powder XRD data. The solid-solution model yields a small $R_{\rm w}$ of 3.65% with a Ba:Sn ratio of ~60:40 and a Zr:Ti ratio of ~50:50, consistent with the average composition of the particles. The refined lattice parameter of 4.0927(1) Å also matches the previously reported value for $(Ba_{0.6}Sn_{0.4})(Zr_{0.5}Ti_{0.5})O_3$. The final R_w for the twophase model is slightly better at 3.55%, with an average Zr:Ti molar ratio of ~50:50. The SZT phase refined to a slightly Zrpoorer fraction, which is consistent with the TEM observations and the formation of small amounts of ZrO₂. The refined BZT and SZT phase fractions were 0.59 (59%) and 0.40 (40%), respectively, consistent with the reaction stoichiometry and TEM observations. A remaining minor phase fraction of 0.01 $(\sim 1\%)$ corresponded to the presence of the ZrO₂ impurity. Furthermore, there was no evidence for the formation of the ilmenite-type SnTiO3 that was recently characterized for the first time. The lattice parameter of the BZT component refined to 4.0963(1) Å, while that of the SZT lattice parameter was found to be slightly smaller at 4.088(1) Å. A slight decrease in the lattice parameter in SZT is consistent with the substitution of the smaller Sn(II) cation for the larger Ba(II)

Several other core—shell materials have previously been investigated via XRD and can serve as a comparison to BZT—SZT. The predominance of prior examples showed a core and

a shell form that constitute two phases that were easily distinguishable using powder XRD methods, unlike the case described above for BZT-SZT. For example, ZnO-ZnS core-shell materials have been reported where ZnO forms in a hexagonal structure while ZnS crystallizes in a cubic structure type.²⁹ The resulting diffraction pattern clearly showed peaks for both materials and made for the unambiguous determination of two distinct phases being present. In another example of CdSe-CdS, more similar to BZT-SZT, both the core and the shell had the same wurtzite structure type. In this case, where both the core and shell crystallize with closely similar lattice parameters, refinements of the resulting diffraction pattern cannot be used to clearly distinguish between one- or two-phase models.³⁰ The CdSe-CdS example is analogous in that both the BZT core and SZT shell are cubic perovskites with similar lattice parameters. Therefore, XRD's inability to distinguish between the core-shell and solid-solution models in this scenario are expected and can be attributed to the fact that the peak intensities of the X-ray diffraction pattern represent an averaged distribution of atomic scattering. The atomic scattering can be represented by an averaged scattering present within a crystalline structure with atomic-site disorder [i.e., (Ba_{0.6}Sn_{0.4})Zr_{0.5}Ti_{0.5}O₃] or the sum of two phases (i.e., $0.6 Ba Zr_{0.5} Ti_{0.5} O_3 - 0.4 Sn Zr_{0.5} Ti_{0.5} O_3).^{31} \ \, \text{In \ \ a \ \, scenario \ \, where}$ the core and shell have the same structure and practically identical lattice parameters, electron microscopy is useful for distinguishing between a two-phase core-shell model or a onephase model containing atomic-site disorder.

As described above, both the BZT core and SZT shell were found to maintain the perovskite-type structure. The Sn(II)exchanged SZT nanoshell, however, was found to contain many polycrystalline domains (Figure 3) that could not be well isolated and indexed by selected area electron diffraction. Rietveld refinements of the BZT and SZT phase fractions in the two-phase model were consistent with the expected loaded stoichiometry for a crystalline SZT nanoshell with a perovskitetype structure. As a test of the sensitivity of the refinements to the presence of Sn in the structural model, refinements of the disordered model of (Ba_{0.6}Sn_{0.4})(Zr_{0.5}Ti_{0.5})O₃ were attempted in which the Ba:Sn A-site occupancy ratio was fixed to 100:0. These resulted in an R_w of ~11%. Next, the Ba:Sn ratio was allowed to refine, yielding a significantly smaller R_w of ~4% and a Ba:Sn ratio of ~60:40. The combined results of the XRD and TEM measurements thereby showed the highest consistency with a polycrystalline SZT nanoshell over a BZT core, with both phases having a cubic perovskite-type structure and nearly identical lattice parameters. Further questions that probed below include the oxidation state of Sn(II) versus



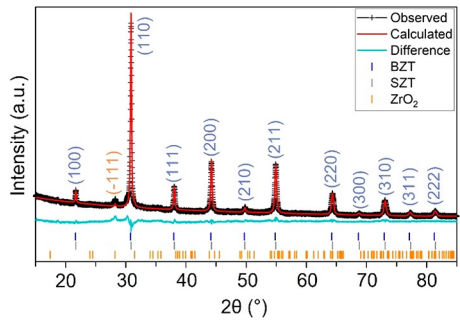


Figure 4. Rietveld refinement plots of the measured diffraction pattern compared to (left) the disordered BSZT model and (right) the BZT-SZT core-shell model. Miller indices for the perovskite(s) and ZrO₂ are labeled in blue/blue gray and orange, respectively.

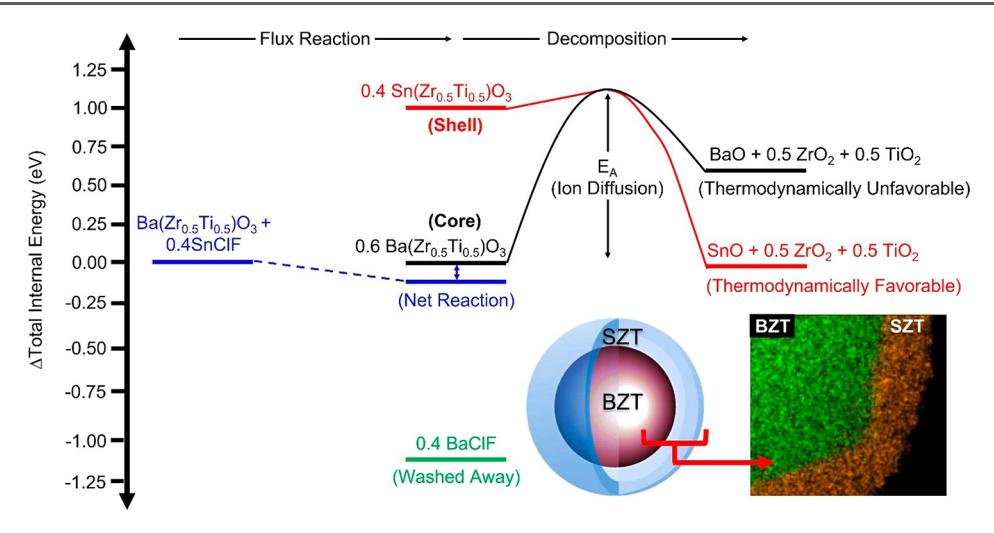


Figure 5. Energetic schematic of the formation of the SZT as a nanoshell covering a BZT particle, i.e., $Ba(Zr_{0.5}Ti_{0.5})O_3 + 0.4SnClF \rightarrow 0.4Sn(Zr_{0.5}Ti_{0.5})O_3 + 0.6Ba(Zr_{0.5}Ti_{0.5})O_3 + 0.4BaClF$, followed by the decomposition pathway to the ground state to give BaO, SnO, ZrO_2 , and TiO_2 .

Sn(IV), the potential structural displacement of the Sn(II) cation arising from its stereoactive lone pair, and the changes in the optical absorption and band gap.

IIIb. Energetics of Forming a Nanoshell of Metastable **SZT.** While the preparation of Sn(II)-containing perovskite oxides, e.g., $Sn(Zr_{0.5}Ti_{0.5})O_3$ (SZT), has represented a wellestablished and synthetically intractable problem, the underlying thermodynamics have not been fully explored. Using prior published procedures, 8,24,25 the thermodynamics of the BZT-SZT reaction are depicted in Figure 5. These data are plotted as a change in total internal energy as compared to the reactants BZT and 0.4SnClF. As illustrated, formation of SZT is highly energetically uphill as compared to that of BZT by +1000 meV formula⁻¹. The energetic penalty to form SZT is thermodynamically offset by the formation of BaClF from SnClF of −1120 meV formula⁻¹. Therefore, the net reaction for the formation of the BZT-SZT core-shell particle is favorable by $-120 \text{ meV formula}^{-1}$. In situ PXRD, which shows the spontaneous formation of BaClF upon the melting of SnClF, supports these calculations that the formation of BaClF is exothermic and drives the formation of SZT. As expected, SZT is metastable toward decomposition to the simpler oxides. The calculated metastability for SZT in this reaction is equivalent to approximately +500 meV atom⁻¹, which is much greater than the prior highest achieved metastability of approximately +300 meV atom⁻¹.8 Furthermore, the calculated metastability of SZT reflects the experimental evidence that shows heating BZT-SZT above the synthesis temperature of 350 °C leads SZT to decompose to its binary oxides.8

Given the energetically favorable pathway for the decomposition of SZT, there must be a substantial kinetic stabilization that facilitates its formation. Its kinetic stabilization can likely be attributed to two key factors. The first is that the large lattice cohesive energy of the BZT precursor enables the B–O substructure to be stabilized during the cation-exchange reaction. As discussed in recent computational studies, the intuitive idea is that stronger bonds lead to a greater ability to "lock in" higher-energy atomic configurations. This concept was formulated after an analysis of ~30000 compounds in the Materials Project Database that found that the most synthesizable metastable compounds tend to be those with high lattice cohesive energies. The high cohesive

energies of these perovskites are reflected in their high melting points, e.g., 1618 °C for BaTiO₃ and 2705 °C for BaZrO₃, 33,6 where the melting point is directly related to the lattice cohesive energy through Lindemann's criterion for melting.³⁵ The second factor is that the low synthesis temperature significantly hinders the requisite ion diffusion that is required for SZT decomposition. As SZT is metastable versus a ground state consisting of its binary oxides SnO, TiO2, and ZrO2, there is a significant amount of atomic diffusion and/or rearrangement that must occur to enable this phase segregation. The necessity for this atomic diffusion on the bulk scale, combined with the relatively low synthesis temperature, serves to kinetically stabilize the SZT nanoshells. Similar to the concept of increasing the lattice cohesive energy, metastable compounds that decompose via phase segregation have been shown to have an increased synthesizability, thus a higher degree of metastability, compared to those that simply undergo a polymorphic transformation.³² Taken together, these concepts can help to identify and unlock the pathways to metastable compounds that might otherwise be considered too thermodynamically unstable to represent viable synthetic

IIIc. Spectroscopic Characterization. In addition to the result of a decreased thermodynamic stability, the exchange of Ba(II) for Sn(II) cations on the A site of the A(Zr_{0.5}Ti_{0.5})O₃ perovskite oxide could potentially be expected to yield subtle changes to the local coordination environments, as well as possible changes in the oxidation states [i.e., Sn(II) vs Sn(IV)] and/or modulation of its optical properties. For example, the stereoactive lone pair of the Sn(II) cation has been predicted in many prior theoretical studies to yield a distortion of its local coordination environment in the perovskite structure. 10-12 In addition, the Sn(II) cation has been found to be relatively easily oxidized at the surfaces upon exposure to water.³⁶ Conversely, the higher energies of the 5s² electrons of the Sn(II) cation have previously been shown to yield significantly smaller band gaps and visible-light photocatalytic activity for water-splitting reactions. To probe and more deeply understand these changes within the SZT nanoshells, 119Sn Mössbauer, UV-vis diffuse reflectance, and X-ray photoelectron spectroscopy were employed on the BZT-SZT coreshell particles.

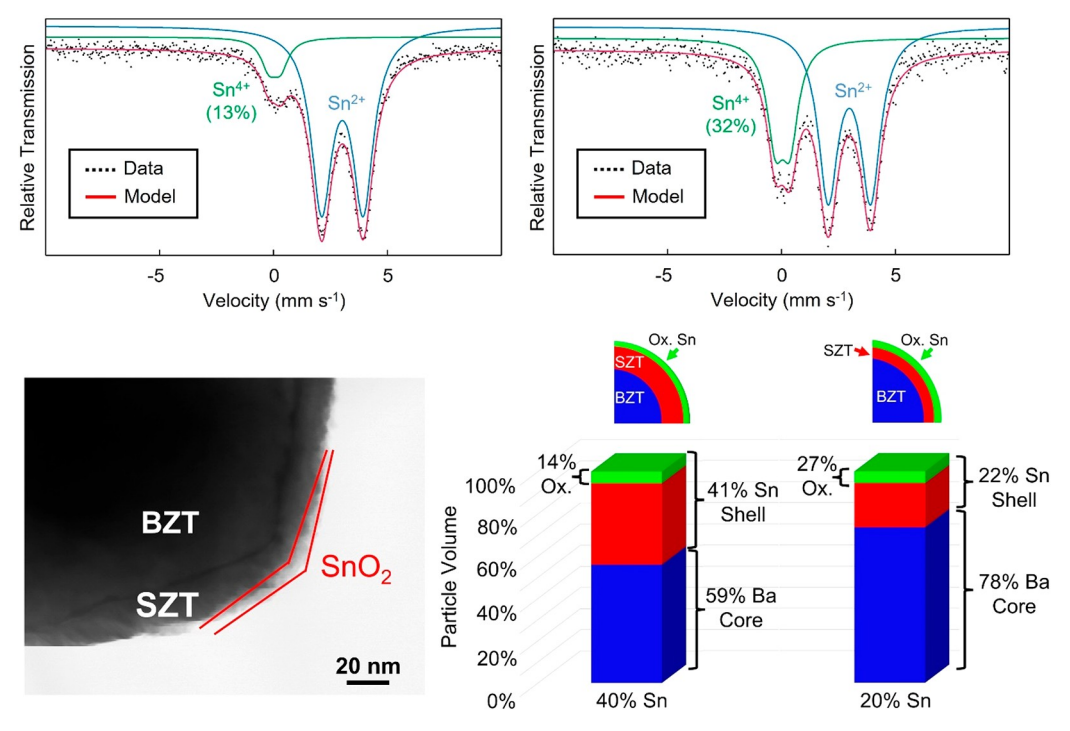


Figure 6. 119 Sn Mössbauer spectra for BZT–SZT products with 40% Sn (top left) and 20% Sn (top right) loading in the reaction, showing the relative molar fractions of Sn(II) and Sn(IV) cations. At the bottom left is a high-resolution TEM image of the outer surface of the SZT shell with a thin amorphous layer that contains oxidized Sn(IV) cations, and at the bottom right are the calculated molar fractions of the BZT core, SZT shell, and oxidized outer layer assuming a 1 μ m diameter spherical particle and a 10 nm oxidation layer. The SZT thickness was 80 and 40 nm for 40% Sn and 20% Sn, respectively, which is consistent with the Mössbauer spectroscopic data.

The oxidation state of Sn was investigated using 119Sn Mössbauer spectroscopy, as shown in the spectra in Figure 6, for flux reactions loaded with 20% and 40% Sn. The 20% Sn composition was prepared to serve as a comparison to the 40% Sn composition. The fitted parameters to the spectra are listed in Table S1. The data show the presence of both Sn(IV) and Sn(II), with the majority of the signal corresponding to Sn(II) cations in each sample. This confirms that the Sn remains predominantly in the +2 oxidation state after undergoing the flux-exchange reaction. The minority Sn(IV) fraction in each is attributed to surface oxidation of Sn(II) cations that occurs during the washing step to remove the BaClF side products. This is consistent with prior studies on ilmenite-type SnTiO₃, which was likewise ascribed to surface oxidation from washing with deionized water.³⁶ The TEM image of the SZT surface, shown in Figure 6 (bottom left), revealed a thin ~5-10 nm amorphous layer that can be attributed to the partial oxidation of the Sn(II) cations in the near-surface regions of the particles. EDS maps and a line scan for the image are shown in Figure S3. This amorphous layer of oxidation appears to be surface limited, while the subsurface SZT remains unoxidized as Sn(II) and polycrystalline.

The observed increase in the Sn(IV) fraction from 13% to 32% correlates inversely with the amount of Sn(II) loaded into the sample, i.e., for the thicker (40% Sn) and thinner (20% Sn) SZT shells, respectively. As a greater amount of Sn(II) is exchanged into the BZT core, the SZT shell extends deeper into the particle and leads to a decrease in the fraction of Sn present at the surface that can be oxidized. The extent of surface oxidation was modeled using the calculated volume fractions of a spherical particle (1 μm diameter), yielding the results shown in Figure 6 (bottom right). For the 40% Sn and 20% Sn BZT–SZT particles, shell thicknesses of 80 and 40 nm

were used, respectively, while a 10 nm oxidation layer was assumed for both, consistent with the TEM data. This yielded calculated volume fractions of the SZT shell and BZT core, which were closely consistent with the experimentally determined ratios. The calculated volume fraction of the Sn(IV) in the oxidized surface region was calculated to be \sim 14% for the 40% Sn-loaded sample and \sim 27% for the 20% Sn-loaded sample. These surface fractions closely match the measured Sn(IV) and Sn(II) fractions from the Mössbauer spectroscopic data. Thus, the larger amount of oxidized Sn(IV) cations in the 20% Sn-loaded SZT-BZT sample arises because of its greater fraction exposed at the surfaces in the thinner SZT shells, showing the oxidation of Sn(II) is surface restricted rather than extending into the bulk. Alternately, if the oxidation of Sn(II) occurred throughout the bulk of the particles, then the 40% Sn-loaded samples would show the largest amount of Sn(IV). However, this is in contradiction with the Mössbauer spectroscopic data.

The observed quadrupole splitting in the ¹¹⁹Sn Mössbauer spectroscopic data, shown in Table S1, also suggested that the Sn(II) coordination is likely slightly distorted within the A site of the perovskite-type structure. Recent reports on the exchange of Sn(II) cations into a layered Ba perovskite show the preference for the Sn(II) cations to occupy asymmetric coordination sites to accommodate its stereoactive lone pair.³⁷ On the basis of the ¹¹⁹Sn Mössbauer data and the literature, it is perhaps likely that SZT actually crystallizes as a pseudocubic structure rather than an ideal cubic perovskite, with minor random displacements of the Sn(II) cation. A possible explanation for the presence of the Sn(II) lone pair within the structure is that the smaller Sn(II) cation (~0.93 Å) sits within an A site vacated by the larger Ba cation (1.36 Å), which in turn allows the Sn(II) cation to undergo a displacement to

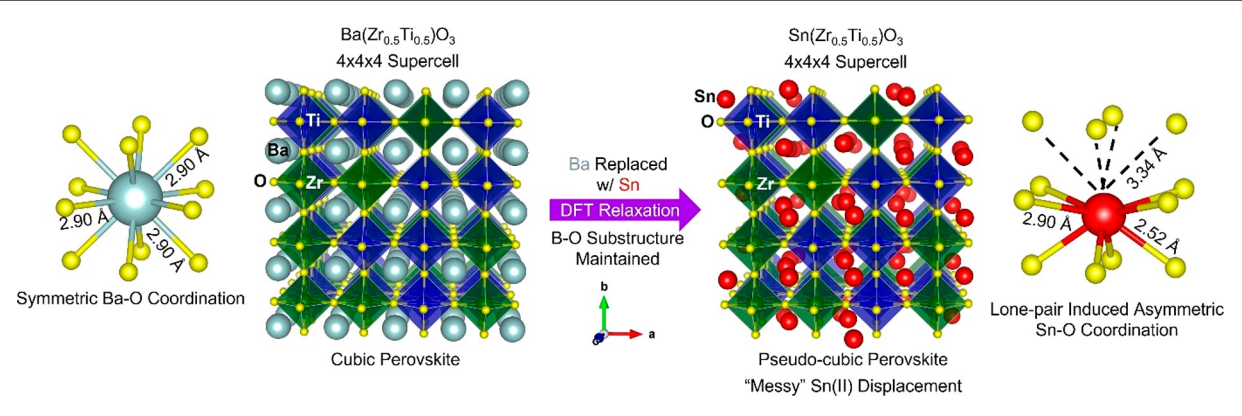


Figure 7. BZT structure as a cubic perovskite determined from Rietveld refinement of X-ray diffraction data shown as a $4 \times 4 \times 4$ supercell where the Ba cations have symmetric 12-fold coordination to O (left). The BZT structure served as the starting model for SZT DFT relaxation. DFT-relaxed SZT structure as a pseudocubic perovskite showing random Sn(II) displacement that is induced by its stereoactive lone pair (right). Only Sn atoms were allowed to move while the B-O substructure was left unaltered from the BZT parent structure.

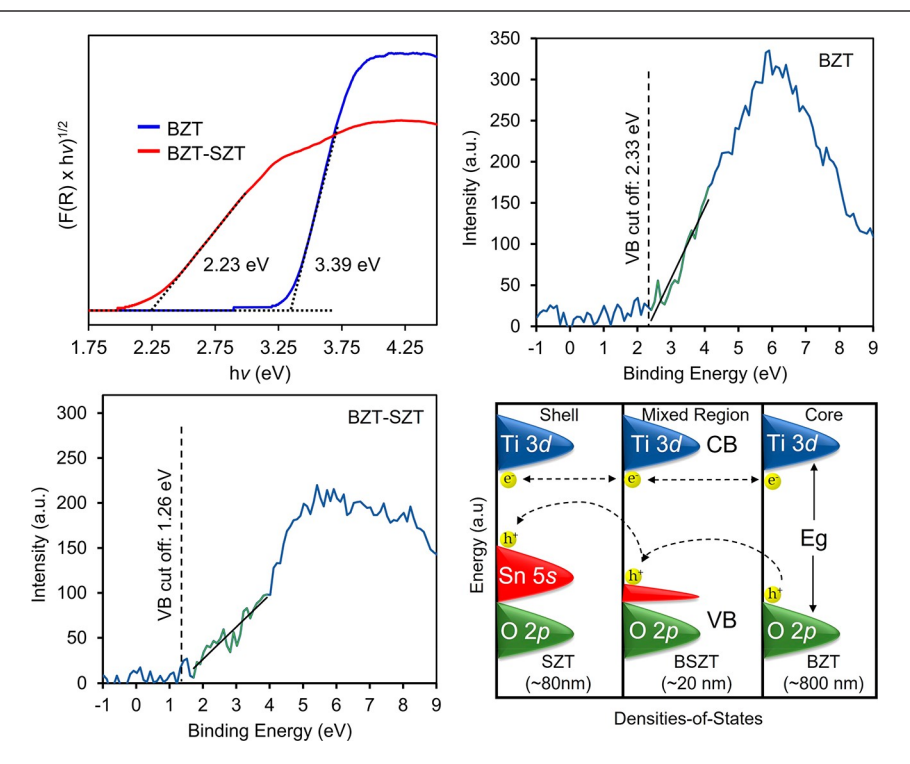


Figure 8. Tauc plots of UV—vis DRS data for pure BZT and core—shell BZT—SZT particles for the indirect band gap transition (top left), their respective valence band edge spectra (top right and bottom left; the data points used for fitting the valence band cutoff are colored green), and schematic of the densities-of-states diagrams as the conduction and valence bands are aligned among the SZT shell, mixed region, and BZT core (bottom right).

better accommodate its lone pair. Geometry relaxations of the cubic SZT structure using DFT methods showed random distortions of the Sn(II) cations, as illustrated in Figure 7 for one example. Generally, these displacements had relatively small to no energetic impact on the total energy, with random distortions leading to its observed pseudocubicity. A relatively flat energetic landscape of randomly displaced Sn(II) cations is thus observed within the perovskite structure.

The BZT-SZT core-shell particles exhibit an orange color after the Sn(II)-exchange reactions, suggesting a significant red-shift of its band gap into the visible regions that is consistent with prior reports. Optical UV-vis diffuse reflectance measurements were taken on powdered samples to determine the band gaps of the starting BZT and BZT-SZT core-shell particles. As shown in Figure 8, both Tauc plots

show that the lowest-energy band gap transitions are indirect with respective values of ~3.39 and ~2.23 eV. Thus, the outer shell of SZT has a band gap that has been red-shifted by ~1.2 eV. To probe the origins of the change in its band gap, valence band XPS data were measured for both BZT and BZT-SZT (illustrated in Figure 8). The valence band cutoffs were determined by extrapolating the slopes of the intensity to the baseline. These data show that the energy of the valence band edge of BZT-SZT has been shifted to higher energies by ~1.07 eV compared to that of pure BZT. This measured difference in the edges of the valence bands is nearly equal to, within error, the change in band gap measured by UV-vis diffuse reflectance. Thus, this result supports prior calculations, showing that the nature of the reduced band gap energy of the Sn(II)-containing compounds is derived from an increase in

the valence band energy as a consequence of the new Sn 5s/O 2p antibonding interactions. ^{38,39}

The resultant band edge positions suggest a likely mechanism for enhanced charge separation of the lightgenerated excitons within core-shell BZT-SZT particles, as illustrated in Figure 8 (bottom left). As confirmed by the valence band XPS, the valence band energy of the SZT shell is significantly higher than that of the BZT core. Therefore, photogenerated holes will potentially be preferentially driven to the SZT shell at the surface where they can be used to drive oxidation reactions, such as molecular oxygen from water. Additionally, because the conduction bands of the BZT core and SZT shell are both derived from the same Ti 3d states, their conduction bands are at essentially closely similar energies. Because of the n-type nature of SZT, as described previously,8 the band bending at the semiconductor-electrolyte interface will likely cause electrons to diffuse from the surface within the depletion region. While applicable to BZT-SZT, this strategy of fabricating core-shell particles to drive an effective separation of electrons or holes is potentially applicable to many other combinations of semiconductor photocatalysts.

IV. CONCLUSIONS

A Sn(II) perovskite oxide, $Sn(Zr_{0.5}Ti_{0.5})O_3$, has been synthesized for the first time in the form of a nanoshell over a Ba(Zr_{0.5}Ti_{0.5})O₃ core. The presence of the perovskite SZT shell was probed via X-ray diffraction and TEM/EDS methods. The Sn(II) perovskite is highly metastable with respect to its more stable binary oxides by +0.500 eV atom⁻¹. Despite the thermodynamic instability, the successful synthesis of SZT is attributed to the strong kinetic stabilization afforded by the high lattice cohesive energy of the underlying perovskite "BO₃" substructure, as well as the kinetic barriers to cation diffusion that would be required for decomposition to take place. The low reaction temperatures, enabled by the low-melting SnClF flux, help facilitate this kinetic stabilization by suppressing cation diffusion during the exchange reaction. 119Sn Mössbauer spectroscopy confirmed the oxidation state of Sn to be predominantly +2, while surface oxidation leads to a thin layer of Sn(IV). Compared to the parent BZT, the new SZT has a red-shifted band gap of ~1.16 eV down to ~2.23 eV that can facilitate new visible-light absorption. This observed red-shift was attributed to the insertion of a higher-energy valence band as found by valence band photoelectron spectroscopy. The higher-energy valence band of the surface SZT can lead to a strong driving force for photogenerated holes to reach the particle surface to drive oxidation reactions. The successful synthesis of SZT reveals a generalizable strategy for the preparation of functional and highly metastable oxides.

ASSOCIATED CONTENT

Supporting Information

The Supporting Information is available free of charge at https://pubs.acs.org/doi/10.1021/acs.chemmater.2c02192.

Additional TEM images, EDS maps, and line scans of BZT-SZT core-shell particles and the ¹¹⁹Sn Mössbauer spectroscopy fitting parameters (PDF)

AUTHOR INFORMATION

Corresponding Author

Paul A. Maggard — Department of Chemistry, North Carolina State University, Raleigh, North Carolina 27696-8204, United States; © orcid.org/0000-0002-3909-1590; Email: Paul Maggard@ncsu.edu

Authors

- Shaun O'Donnell Department of Chemistry, North Carolina State University, Raleigh, North Carolina 27696-8204, United States
- D. J. Osborn Department of Chemistry, The University of Adelaide, Adelaide, South Australia 5005, Australia
- Gowri Krishnan Flinders Institute for Nanoscale Science and Technology, Flinders University, Adelaide, South Australia 5001, Australia
- Theresa Block Institut für Anorganische und Analytische Chemie, Universität Münster, 48149 Münster, Germany
- Aylin Koldemir Institut für Anorganische und Analytische Chemie, Universität Münster, 48149 Münster, Germany
- Thomas D. Small Department of Chemistry, The University of Adelaide, Adelaide, South Australia 5005, Australia
- Rachel Broughton Department of Materials Science and Engineering, North Carolina State University, Raleigh, North Carolina 27695-8204, United States
- Jacob L. Jones Department of Materials Science and Engineering, North Carolina State University, Raleigh, North Carolina 27695-8204, United States; ⊚ orcid.org/0000-0002-9182-0957
- Rainer Pöttgen Institut für Anorganische und Analytische Chemie, Universität Münster, 48149 Münster, Germany
- Gunther G. Andersson Flinders Institute for Nanoscale Science and Technology, Flinders University, Adelaide, South Australia 5001, Australia; orcid.org/0000-0001-5742-3037
- Gregory F. Metha Department of Chemistry, The University of Adelaide, Adelaide, South Australia 5005, Australia; orcid.org/0000-0003-1094-0947

Complete contact information is available at: https://pubs.acs.org/10.1021/acs.chemmater.2c02192

Notes

The authors declare no competing financial interest.

ACKNOWLEDGMENTS

The authors acknowledge primary support of this work from the National Science Foundation (DMR-2004455). Additional components of this research were performed in part at the Analytical Instrumentation Facility (AIF) at North Carolina State University, which is supported by the State of North Carolina and the National Science Foundation (Grant ECCS-2025064). The AIF is a member of the North Carolina Research Triangle Nanotechnology Network (RTNN), a site in the National Nanotechnology Coordinated Infrastructure (NNCI). Parts of this research were also performed as part of the Australian Solar Thermal Research Institute (ASTRI), a project supported by the Australian Government, through the Australian Renewable Energy Agency (ARENA). The authors acknowledge the facilities, and the scientific and technical assistance, of Ashley Slattery with Microscopy Australia (formerly known as AMMRF) at the University of Adelaide and the Australian National Fabrication Facility (ANFF) at

Flinders University. The authors acknowledge Flinders Microscopy and Microanalysis and their expertise.

REFERENCES

- (1) Liu, C.; Zhou, W.; Zhang, J.; Chen, Z.; Liu, S.; Zhang, Y.; Yang, J.; Xu, L.; Hu, W.; Chen, Y.; Deng, Y. Air-Assisted Transient Synthesis of Metastable Nickel Oxide Boosting Alkaline Fuel Oxidation Reaction. *Adv. Energy Mater.* **2020**, *10* (46), 2001397.
- (2) Duan, Y.; Sun, S.; Sun, Y.; Xi, S.; Chi, X.; Zhang, Q.; Ren, X.; Wang, J.; Ong, S. J. H.; Du, Y.; et al. Mastering Surface Reconstruction of Metastable Spinel Oxides for Better Water Oxidation. *Adv. Mater.* **2019**, *31* (12), 1807898.
- (3) Hiley, C. I.; Lees, M. R.; Fisher, J. M.; Thompsett, D.; Agrestini, S.; Smith, R. I.; Walton, R. I. Ruthenium(V) Oxides from Low-Temperature Hydrothermal Synthesis. *Angew. Chem.* **2014**, *126* (17), 4512–4516.
- (4) Bartel, C. J.; Sutton, C.; Goldsmith, B. R.; Ouyang, R.; Musgrave, C. B.; Ghiringhelli, L. M.; Scheffler, M. New Tolerance Factor to Predict the Stability of Perovskite Oxides and Halides. *Sci. Adv.* **2019**, 5 (2), aav0693.
- (5) Parija, A.; Waetzig, G. R.; Andrews, J. L.; Banerjee, S. Traversing Energy Landscapes Away from Equilibrium: Strategies for Accessing and Utilizing Metastable Phase Space. *J. Phys. Chem. C* **2018**, *122* (45), 25709–25728.
- (6) Hu, Y.; Yao, X.; Schlom, D. G.; Datta, S.; Cho, K. First Principles Design of High Hole Mobility p-Type Sn-O-X Ternary Oxides: Valence Orbital Engineering of Sn²⁺ in Sn²⁺-O-X by Selection of Appropriate Elements X. Chem. Mater. **2021**, 33 (1), 212–225.
- (7) Hautier, G.; Miglio, A.; Ceder, G.; Rignanese, G. M.; Gonze, X. Identification and Design Principles of Low Hole Effective Mass p-Type Transparent Conducting Oxides. *Nat. Commun.* **2013**, *4*, 2292.
- (8) O'Donnell, S.; Chung, C. C.; Carbone, A.; Broughton, R.; Jones, J. L.; Maggard, P. A. Pushing the Limits of Metastability in Semiconducting Perovskite Oxides for Visible-Light-Driven Water Oxidation. *Chem. Mater.* **2020**, 32 (7), 3054–3064.
- (9) Gabilondo, E. A.; O'Donnell, S.; Broughton, R.; Jones, J. L.; Maggard, P. A. Synthesis and Stability of Sn(II)-Containing Perovskites: (Ba,Sn^{II})Hf^{IV}O₃ versus (Ba,Sn^{II})Sn^{IV}O₃. *J. Solid State Chem.* **2021**, 302, 122419.
- (10) Parker, W. D.; Rondinelli, J. M.; Nakhmanson, S. M. First-Principles Study of Misfit Strain-Stabilized Ferroelectric SnTiO $_3$. *Phys. Rev. B* **2011**, *84*, 245126.
- (11) Ribeiro, R. A. P.; de Lazaro, S. R. DFT/PBE0 Study on Structural, Electronic and Dielectric Properties of SnZr_{0.50}Ti_{0.50}O₃ Lead-Free Ferroelectric Material. *J. Alloys Compd.* **2017**, 714, 553–559.
- (12) Gardner, J.; Thakre, A.; Kumar, A.; Scott, J. F. Tin Titanate The Hunt for a New Ferroelectric Perovskite. *Rep. Prog. Phys.* **2019**, 82 (9), 092501.
- (13) Gauzzi, F.; Verdini, B.; Maddalena, A.; Principi, G. X-Ray Diffraction and Mössbauer Analyses of SnO Disproportionation Products. *Inorg. Chim. Acta* **1985**, *104* (1), 1–7.
- (14) Campo, C. M.; Rodríguez, J. E.; Ramírez, A. E. Thermal Behaviour of Romarchite Phase SnO in Different Atmospheres: A Hypothesis about the Phase Transformation. *Heliyon* **2016**, 2 (5), e00112.
- (15) Diehl, L.; Bette, S.; Pielnhofer, F.; Betzler, S.; Moudrakovski, I.; Ozin, G. A.; Dinnebier, R.; Lotsch, B. V. Structure-Directing Lone Pairs: Synthesis and Structural Characterization of SnTiO₃. *Chem. Mater.* **2018**, *30* (24), 8932–8938.
- (16) Toby, B. H.; Von Dreele, R. B. GSAS-II: The Genesis of a Modern Open-Source All Purpose Crystallography Software Package. *J. Appl. Crystallogr.* **2013**, 46 (2), 544–549.
- (17) Simmons, E. L. Reflectance Spectroscopy: Application of the Kubelka-Munk Theory to the Rates of Photoprocesses of Powders. *Appl. Opt.* **1976**, *15* (4), 951.
- (18) Long, G. J.; Cranshaw, T. E.; Longworth, G. The Ideal Mössbauer Effect Absorber Thickness. *Moessbauer Eff. Ref. Data J.* 1983, No. 6, 42–49.

- (19) Brand, R. A. WinNormos for Igor6 (Version for Igor 6.2 or above: 22/02/2017); Universität Duisburg: Duisburg, Germany, 2017.
- (20) Ellis, A. V.; Al-Deen, A.; Dalal, H.; Andersson, G. G. Structural Determination of Thermally and Hydrazine Treated Graphene Oxide Using Electron Spectroscopic Analysis. *J. Phys. Chem. C* **2013**, *117* (41), 21312–21319.
- (21) Acres, R. G.; Ellis, A. V.; Alvino, J.; Lenahan, C. E.; Khodakov, D. A.; Metha, G. F.; Andersson, G. G. Molecular Structure of 3-Aminopropyltriethoxysilane Layers Formed on Silanol-Terminated Silicon Surfaces. *J. Phys. Chem. C* **2012**, *116* (10), 6289–6297.
- (22) Kresse, G.; Furthmüller. Efficiency of Ab-Initio Total Energy Calculations for Metals and Semiconductors Using a Plane-Wave Basis Set. *Comput. Mater. Sci.* **1996**, *6* (1), 15–50.
- (23) Perdew, J.; Burke, L.; Ernzerhof, M. Generalized Gradient Approximation Made Simple. *Phys. Rev. Lett.* **1996**, *77*, 3865.
- (24) Hautier, G.; Ong, S. P.; Jain, A.; Moore, C. J.; Ceder, G. Accuracy of Density Functional Theory in Predicting Formation Energies of Ternary Oxides from Binary Oxides and its Implication on Phase Stability. *Phys. Rev. B* **2012**, *85* (15), 155208.
- (25) Emery, A. A.; Wolverton, C. High-Throughput DFT Calculations of Formation Energy, Stability and Oxygen Vacancy Formation Energy of ABO₃ Perovskites. *Sci. Data* **2017**, *4*, 170153.
- (26) Saal, J. E.; Kirklin, S.; Aykol, M.; Meredig, B.; Wolverton, C. Materials Design and Discovery with High-Throughput Density Functional Theory: The Open Quantum Materials Database (OQMD). *Jom* **2013**, *65* (11), 1501–1509.
- (27) Gabilondo, E.; O'Donnell, S.; Newell, R.; Broughton, R.; Mateus, M.; Jones, J.; Maggard, P. A. Renaissance of Topotactic Ion-Exchange for Functional Solids with Close Packed Structures. *Chem. Eur. J.* **2022**, 479, e202200479.
- (28) O'Donnell, S.; Hamilton, A.; Maggard, P. A. Fast Flux Reaction Approach for the Preparation of Sn₂TiO₄: Tuning Particle Sizes and Photocatalytic Properties. *J. Electrochem. Soc.* **2019**, *166* (5), H3084–H3090.
- (29) Yu, Y. X.; Ouyang, W. X.; Liao, Z. T.; Du, B.-B.; Zhang, W. De. Construction of ZnO/ZnS/CdS/CuInS₂ Core-Shell Nanowire Arrays via Ion Exchange: p-n Junction Photoanode with Enhanced Photoelectrochemical Activity under Visible Light. *ACS Appl. Mater. Interfaces* **2014**, *6* (11), 8467–8474.
- (30) Peng, X.; Schlamp, M. C.; Kadavanich, A. V.; Alivisatos, A. P. Epitaxial Growth of Highly Luminescent CdSe/CdS Core/Shell Nanocrystals with Photostability and Electronic Accessibility. *J. Am. Chem. Soc.* **1997**, *119* (30), 7019–7029.
- (31) Jenkins, R.; Snyder, R. L. Introduction to X-ray Powder Diffractometry. In *Chemical Analysis*; John Wiley & Sons, Inc., 1996; Vol. 138.
- (32) Sun, W.; Dacek, S. T.; Ong, S. P.; Hautier, G.; Jain, A.; Richards, W. D.; Gamst, A. C.; Persson, K. A.; Ceder, G. The Thermodynamic Scale of Inorganic Crystalline Metastability. *Sci. Adv.* **2016**, *2* (11), 1600225.
- (33) Guha, J. P.; Kolar, D. Phase Equilibria in the System $BaTiO_3$ - $BaGeO_3$. J. Mater. Sci. **1972**, 7 (10), 1192–1196.
- (34) Yamanaka, S.; Fujikane, M.; Hamaguchi, T.; Muta, H.; Oyama, T.; Matsuda, T.; Kobayashi, S. I.; Kurosaki, K. Thermophysical Properties of BaZrO₃ and BaCeO₃. *J. Alloys Compd.* **2003**, 359 (1–2), 109–113.
- (35) Nanda, K. K.; Sahu, S. N.; Behera, S. N. Liquid-Drop Model for the Size-Dependent Melting of Low-Dimensional Systems. *Phys. Rev.* A 2002, 66 (1), 132081.
- (36) Diehl, L.; Fabini, D. H.; Vargas-Barbosa, N. M.; Jiménez-Solano, A.; Block, T.; Duppel, V.; Moudrakovski, I.; Küster, K.; Pöttgen, R.; Lotsch, B. V. Interplay between Valence Band Tuning and Redox Stability in SnTiO₃: Implications for Directed Design of Photocatalysts. *Chem. Mater.* **2021**, *33* (8), 2824–2836.
- (37) O'Donnell, S.; Smith, A.; Carbone, A.; Maggard, P. A. Structure, Stability, and Photocatalytic Activity of a Layered Perovskite Niobate after Flux-Mediated Sn(II) Exchange. *Inorg. Chem.* **2022**, *61* (9), 4062–4070.

(38) Hosogi, Y.; Kato, H.; Kudo, A. Photocatalytic Activities of Layered Titanates and Niobates Ion-Exchanged with Sn²⁺ under Visible Light Irradiation. *J. Phys. Chem. C* **2008**, *112* (45), 17678–17682.

(39) Zhu, Z.; Sarker, P.; Zhao, C.; Zhou, L.; Grimm, R. L.; Huda, M. N.; Rao, P. M. Photoelectrochemical Properties and Behavior of α -SnWO₄ Photoanodes Synthesized by Hydrothermal Conversion of WO₃ Films. *ACS Appl. Mater. Interfaces* **2017**, 9 (2), 1459–1470.

□ Recommended by ACS

Pushing the Limits of Metastability in Semiconducting Perovskite Oxides for Visible-Light-Driven Water Oxidation

Shaun O'Donnell, Paul A. Maggard, et al.

MARCH 10, 2020

CHEMISTRY OF MATERIALS

READ 🗹

Band Gap-Tunable (Mg, Zn)SnN₂ Earth-Abundant Alloys with a Wurtzite Structure

Naoomi Yamada, Fumio Kawamura, et al.

OCTOBER 20, 2021

ACS APPLIED ELECTRONIC MATERIALS

READ 🗹

First-Principles Study of Intrinsic Point Defects and Optical Properties of $SmNiO_3$

Yuanyuan Cui, Yanfeng Gao, et al.

DECEMBER 28, 2020

THE JOURNAL OF PHYSICAL CHEMISTRY A

READ 🗹

Synthesis of Narrow SnTe Nanowires Using Alloy Nanoparticles

Pengzi Liu, Judy J. Cha, et al.

DECEMBER 30, 2020

ACS APPLIED ELECTRONIC MATERIALS

READ 🗹

Get More Suggestions >